Article

Crystal growth, structural phase transitions and optical gap evolution of CH3NH3Pb(Br1-xClx)3 powders

M.C. Alvarez-Galvan, J.A. Alonso, C.A. Lopez, E. Lopez-Linares, C. Contreras, M.J. Lázaro, F. Fauth, and M.V. Martínez-Huerta

Cryst. Growth Des., **Just Accepted Manuscript** • DOI: 10.1021/acs.cgd.8b01463 • Publication Date (Web): 11 Dec 2018

Crystal growth, structural phase transitions and optical gap evolution of $CH_3NH_3Pb(Br_{1-x}Cl_x)_3$ powders

M.C. Alvarez-Galván[1], J. A. Alonso[2*], C.A. López[3], E. López-Linares[1], C. Contreras[1], M.J. Lázaro[4], F. Fauth[5] and M.V. Martínez-Huerta[1*]

[1] *Instituto de Catálisis y Petroleoquímica, CSIC, Cantoblanco 28049 Madrid, Spain*

[2] *Instituto de Ciencia de Materiales de Madrid, CSIC, Cantoblanco 28049 Madrid, Spain*

[3] *Instituto de Investigaciones en Tecnología Química (INTEQUI), UNSL, CONICET and Facultad de Química, Bioquímica y Farmacia, UNSL, Chacabuco y Pedernera, San Luis, 5700, Argentina.*

[4] *Instituto de Carboquímica, CSIC, Miguel Luesma Castán 4, E50018 Zaragoza, Spain*

[5] *CELLS–ALBA synchrotron, Cerdanyola del Valles, Barcelona, E-08290, Spain*

*ja.alonso@icmm.csic.es; mmartinez@icp.csic.es

Abstract

Chemically tuned inorganic-organic hybrid halide perovskites based on bromide and chloride anions $CH_3NH_3Pb(Br_{1-x}Cl_x)_3$ have been crystallized and investigated by synchrotron X-ray diffraction (SXRD), scanning electron microscopy and UV-vis spectroscopy. $CH_3NH_3PbBr_3$ and $CH_3NH_3PbCl_3$ experience successive phase transitions upon cooling, which are suppressed for intermediate compositions probably due to compositional disorder. For $CH_3NH_3PbCl_3$ a transient phase, formerly described as tetragonal, was identified at 167.5 K; the analysis of SXRD data demonstrated that it is indeed orthorhombic, with space group *Pnma*, and $a \approx \sqrt{2}a_p$; $b \approx 2a_p$; $c \approx \sqrt{2}a_p$ (a_p is the ideal cubic perovskite unit-cell parameter). The band gap engineering brought about by the chemical management of $CH_3NH_3Pb(Br_{1-x}Cl_x)_3$ perovskites can be controllably tuned: the gap progressively increases with the concentration of Cl ions from 2.2 to 2.9 eV, and shows a concomitant variation with the unit-cell parameters of the cubic phases at 295 K. This study provides an improved understanding of the structural and optical properties of the mixed $CH_3NH_3Pb(Br_{1-x}Cl_x)_3$ perovskites.

Keywords: hybrid perovskite, mixed halide, bromine, chlorine, solar cells

1. Introduction

Organic-inorganic hybrid halide perovskites have shown tremendous potential as the absorber layer in third-generation photovoltaic cells technologies that can compete with the well-established silicon solar cells in terms of power conversion efficiency (PCE) and cost. [1] . Over the past years, an intensive research has been devoted to the improvement of halide perovskite-based solar cells, where a variety of cell architectures has been developed, increasing the power conversion efficiencies to 23 %. [2] In addition, the structural and optoelectronic properties of these materials can be easily tuned through compositional engineering of various organic ligands, metals, or halogens.[3-4] By varying their compositions, perovskites with different bandgap energies (E_g) have been successfully employed for other optoelectronic applications such as wave-tunable lasing,[5] light-emitting diodes,[6] photodetectors, [7-8] and photocatalysts.[9]

Halide perovskite compounds include the compositions $MAPbX_3$ ($MA = CH_3NH_3^+$, X = Cl, Br, I). $CH_3NH_3PbI_3$-based perovskite solar cells have been a primary focus due to their near-complete visible light absorption in films <1 μm and their fast charge extraction rates. However, the poor stability of $CH_3NH_3PbI_3$ and rapid degradation in humidity has remained a major obstacle for commercialization.[10] $CH_3NH_3PbBr_3$ is a promising alternative to $CH_3NH_3PbI_3$ with a large band-gap of 2.2 eV, which gives rise to a high open circuit voltage (Voc ≈ 1.2–1.5 V) [11]. Their long exciton diffusion length (>1.2 μm) enables good charge transport in devices. In addition, $CH_3NH_3PbBr_3$ demonstrates higher stability towards air and moisture due to its stable cubic phase and low ionic mobility relative to the pseudocubic $CH_3NH_3PbI_3$, in which inherent lattice strain provides an avenue for increased diffusion.[12] Maculan et al.[8] reported that the trap-state density, charge carrier concentration, mobility, and diffusion length of $CH_3NH_3PbCl_3$ are comparable with those of the best quality crystals of $CH_3NH_3PbI_3$ and $CH_3NH_3PbBr_3$. Furthermore, $CH_3NH_3PbCl_3$ possesses a wide band gap of 3.11 eV and it is visibly transparent but sensitive to the ultraviolet (UV) region. $CH_3NH_3PbCl_3$-based UV photodetectors exhibit high ON−OFF current ratio, fast photoresponse, and long-term photostability. $CH_3NH_3PbCl_3$ can also be used in transparent optoelectronics, fire and missile plume detection, and optical communications. [13] However, $CH_3NH_3PbCl_3$ has been rarely investigated both theoretically and experimentally, as well as

the mixed anion $CH_3NH_3Pb(Br_{1-x}Cl_x)_3$ perovskites.[14] The optimal band gap and suitable structure of the materials are key factors for successful application of organic–inorganic hybrid halide perovskites in optoelectronic devices.

Herein, we performed a systematic study of the structural and optical properties of mixed organic-inorganic hybrid perovskites $CH_3NH_3Pb(Br_{1-x}Cl_x)_3$ by combining synchrotron X-ray diffraction (SXRD), scanning electron microscopy (SEM) and UV-vis spectroscopic measurements.

2. Experimental

The mixed perovskites $CH_3NH_3Pb(Br_{1-x}Cl_x)_3$ (x = 0, 0.33, 0.5, 0.67 and 1) were synthesized from a solution of stoichiometric amounts of CH_3NH_3X and PbX_2 (X = Cl, Br) in dimethyl formamide (DMF).

Synthesis of CH_3NH_3X (X: Br, Cl)

The chemicals used for the synthesis of methyl ammonium bromide and methyl ammonium chloride are methyl amine (CH_3NH_2, Aldrich, 33 % in ethanol) and the corresponding acid: HBr (Alfa Aesar, 48 % in water) and HCl (Sigma-Aldrich, 37 % in water). The molar ratio CH_3NH_2/HX is 1.2. The reaction between both compounds is exothermic, being carried out at 0ºC through a refluxing process. First, CH_3NH_2 is added in a flask and then HX is added dropwise slowly. Then, it is left under stirring for 2 h. Finally, the synthesis is finished by rotary evaporation at 60ºC, by which a white powder is formed[15]. This product is rinsed 3 times with diethyl ether (decanting in between). The product was finally dried in a vacuum drying oven at 55ºC for 12 h and stored in a glove box or in a glass desiccator.

Synthesis of $CH_3NH_3PbX_3$

The synthesis of $CH_3NH_3Pb(Br_{1-x}Cl_x)_3$ (x = 0, 0.33, 0.5, 0.67 and 1) was carried out by reaction between stoichiometric amounts of CH_3NH_3X (X = Cl, Br) and PbX_2 (X = Cl, Br); $PbBr_2$ (Alfa Aesar, ultradry 99,99 %), $PbCl_2$ (Alfa Aesar, ultradry 99,99 %) in N,N

dimethyl formamide (DMF) with a molar ratio CH_3NH_3X/PbX_2 = 1 for all the samples, with the exception of $CH_3NH_3PbCl_3$, for which it was 2. This higher value was chosen in order to shift the reaction to the formation of the perovskite, since, in this case, the thermodynamic equilibrium is not so favored[16]. The synthesized perovskites are named as follow: $MAPbBr_3$, $MAPbBr_2Cl$, $MAPbBr_{1.5}Cl_{1.5}$, $MAPbBrCl_2$ and $MAPbCl_3$.

A closed vial containing the suspension of both compounds in DMF (where the weight of DMF is equal to the sum of the precursors weight) is left under stirring on a hot plate at 60ºC for 22 h. Then, the content is poured on a crystallizer placed on a hot plate at 100ºC for 30 min[16-17]. An orange/yellow powder is obtained (the colour depends on the proportion of bromine, being more orange with a higher proportion of this element).

X-ray diffraction profiles of the powder catalysts were obtained on a PANalytical X'Pert Pro X-ray diffractometer with a Cu Kα source. The samples were additionally studied by synchrotron X-ray powder diffraction (SXRD) in the MSPD high-resolution diffractometer at the ALBA facility, Barcelona (Spain), selecting an incident beam with 38 keV energy, λ= 0.3252 Å with the high angular resolution mode (MAD set-up).[18] The polycrystalline powders were contained in quartz capillaries of 0.3 mm diameter, which were rotating during the acquisition time. SXRD patterns were collected at room temperature (295 K, RT), then cooled to 120 K, and when a phase transition was detected, measured at increasing temperatures along the sequence 150, 180, 210, 240 and 270 K. For $MAPbCl_3$, additional patterns were collected at 160, 165, 167.5, 170, 172.5, and 175 K. The refinement of the structures was performed by the Rietveld method using the Fullprof software.[19] There were no regions excluded in the refinement. The following parameters were refined: zero-point error; scale factor; background coefficients; pseudo-Voigt shape parameters; occupancy of the elements; atomic coordinates; and anisotropic displacements for the metal and halogen atoms.

The Scanning Electron Microscope images were obtained on a Hitachi instrument, model TM-1000. The optical diffuse reflectance spectra of perovskites powder were measured at room temperature using a UV-VIS spectrophotometer Varian Cary 5000.

3. Results and Discussion

3.1. *Crystal growth*

The $CH_3NH_3PbX_3$ (X = Cl, Br) perovskites were obtained as crystalline materials, exhibiting crystals of variable sizes and colors, varying from orange for $CH_3NH_3PbBr_3$ to white for $CH_3NH_3PbCl_3$, adopting progressively paler hues of yellow as Cl contents increases, as shown in the optical microscope images included in Fig. 1.

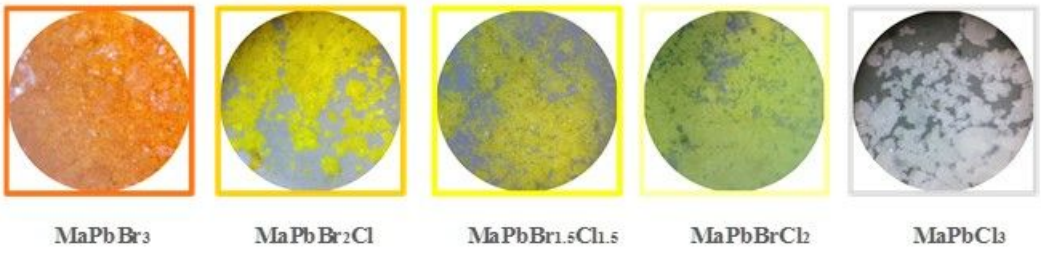

Fig. 1. Optical microscope images of as-grown $CH_3NH_3PbX_3$ (X = Cl, Br) perovskites, showing the color variation as Cl is introduced.

SEM images were obtained to better understand the effect of halide composition on the morphology and structure of crystals (Fig. 2). In all cases, the obtained perovskites show cuboid-type microcrystals. A second morphology, approaching parallelepiped crystals is observed for $CH_3NH_3PbBrCl_2$, whereas some shapeless polycrystalline material is observed for $CH_3NH_3PbBr_2Cl$. No clear trend is observed between the size of the crystals of the mixed perovskites and the content of chloride (x in $CH_3NH_3Pb(Br_{1-x}Cl_x)_3$).

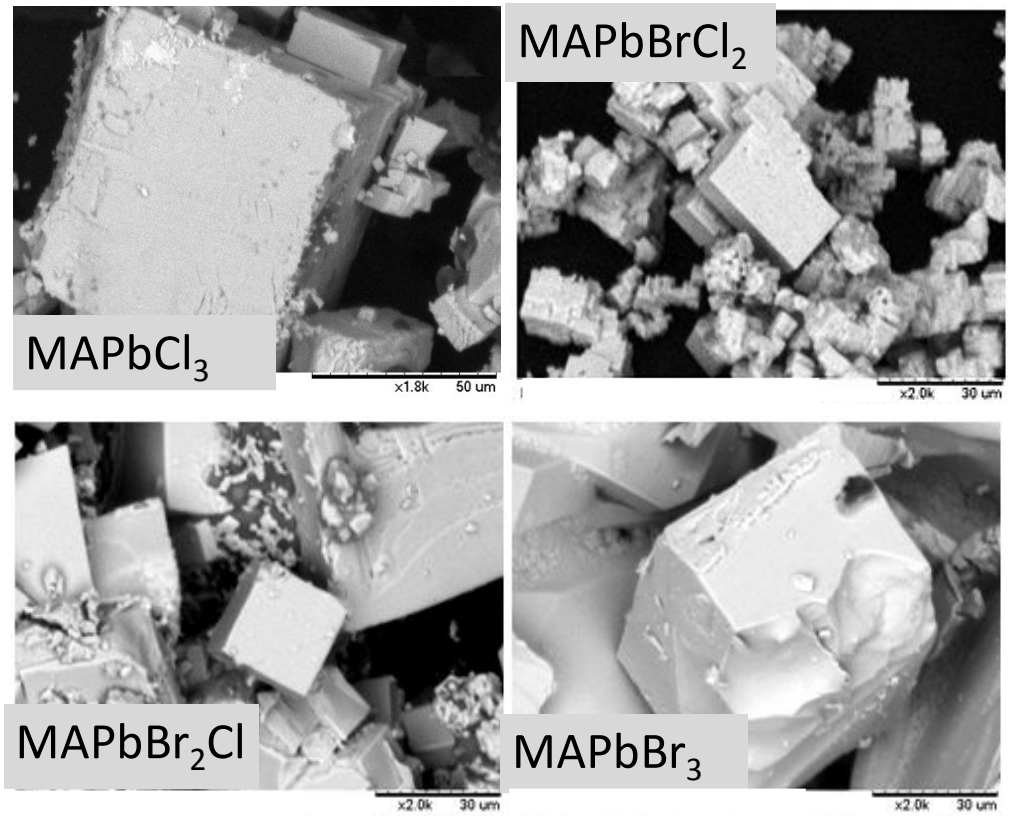

Fig. 2. SEM images of the mixed perovskites

3.2 *Structural characterization*

The structural investigation was performed from SXRD data. The extreme angular resolution of the patterns is essential to accurately define the symmetry of the different mixed phases and to determine its evolution below room temperature (RT). In all cases, the crystal structures at RT are cubic and can be defined in the space group $Pm\bar{3}m$. Fig. 3 shows a Le Bail fit of the SXRD data of the end member $CH_3NH_3PbBr_3$ in the mentioned space group. A thorough structural study in combination with neutron diffraction data was described elsewhere[11] for this end member, showing a disordered configuration of $CH_3NH_3^+$ organic cation in the cage of the cubic perovskite. At ambient temperature, the C and N atoms are delocalized at large multiplicity sites, alternating between six different positions all aligned along [110] direction, as illustrated in Fig. 3.

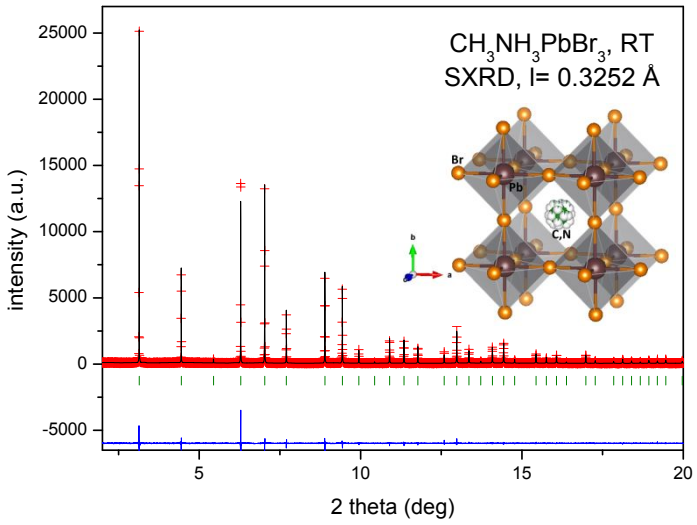

Fig. 3. SXRD profiles for $CH_3NH_3PbBr_3$ at RT, after a pattern matching showing the characteristic perovskite peaks and the absence of impurities. Red crosses are the experimental points, the black full line is the calculated profile and the blue lower line is the difference. The green vertical marks represent the allowed Bragg positions in the $Pm\bar{3}m$ space group, with a= 5.93114(6) Å. [11]

Fig. 4 shows the Rietveld refinements corresponding to x = 0.33 to 1 perovskites at RT. Minor amounts of $PbCl_2$ and MACl were identified and included in the refinements as second and third phases. Table 1 lists the main crystallographic parameters and the reliability factors after Rietveld refinements.

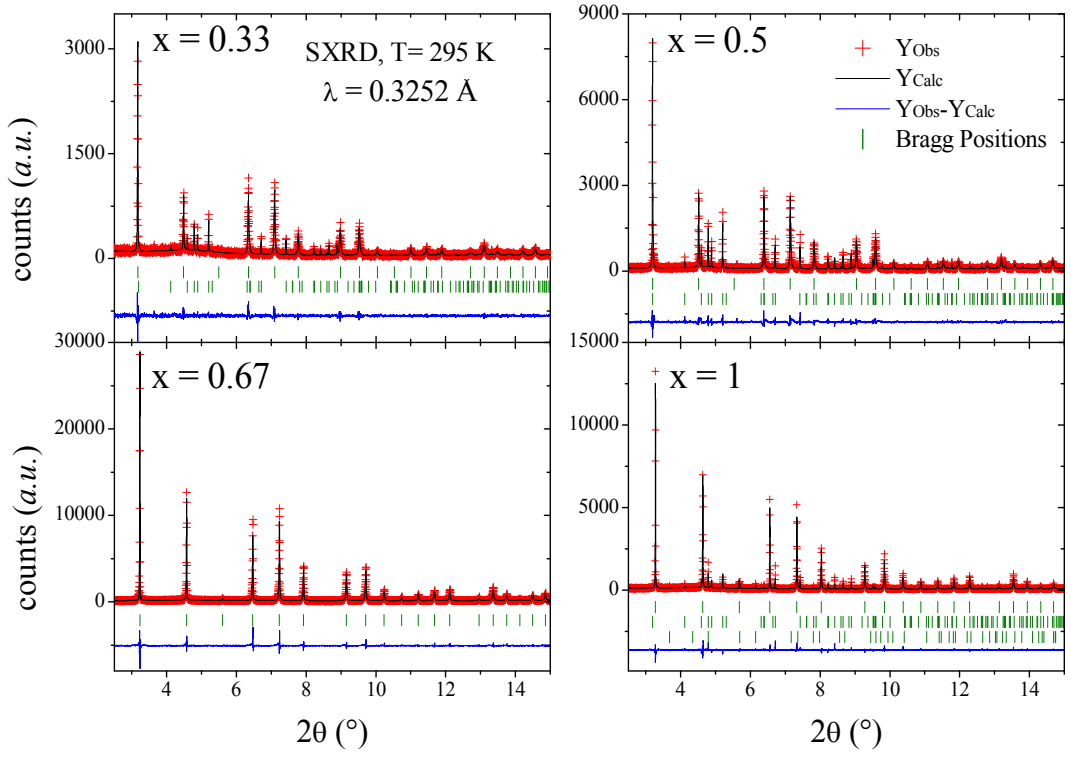

Figure 4. SXRD profiles for $CH_3NH_3Pb(Br_{1-x}Cl_x)_3$ (x = 0.33, 0.5, 0.67 and 1) at RT, after a Rietveld refinement of the perovskite crystal structures. Red crosses are the experimental points, the black full line is the calculated profile and the blue lower line is the difference. The green vertical marks represent the allowed Bragg positions in the $Pm\bar{3}m$ space group; the second and third series of marks correspond to $PbCl_2$ and MACl.

Fig. 5 plots the unit-cell parameter variation and the anisotropic atomic displacement parameters (ADP) of the X ion. The unit-cell parameters exhibit a reduction as the amount of Cl increases, as expected, but this change is not linear; the slope additionally increases beyond x= 0.5; i.e. $MAPbBr_{1.5}Cl_{1.5}$. The ADPs of X atoms are significantly anisotropic, as shown in the insets of Fig. 5, showing an oblate-type consisting of flattened disks perpendicular to the Pb-X-Pb chemical bonds. This is the usual configuration in perovskites, where the thermal vibrations are preferentially permitted in this direction: an oblate spheroid locks the halogen atoms at mid-lead positions with enhanced vibrations perpendicular to the Pb-Pb distance. On the other hand, the ADPs for intermediate mixed halide phases (x = 0.33, 0.5 and 0.67) present a non-monotonic variation in comparison

with both end members (x = 0 and 1), although the difference does not overcome two times the standard deviations and are less significant.

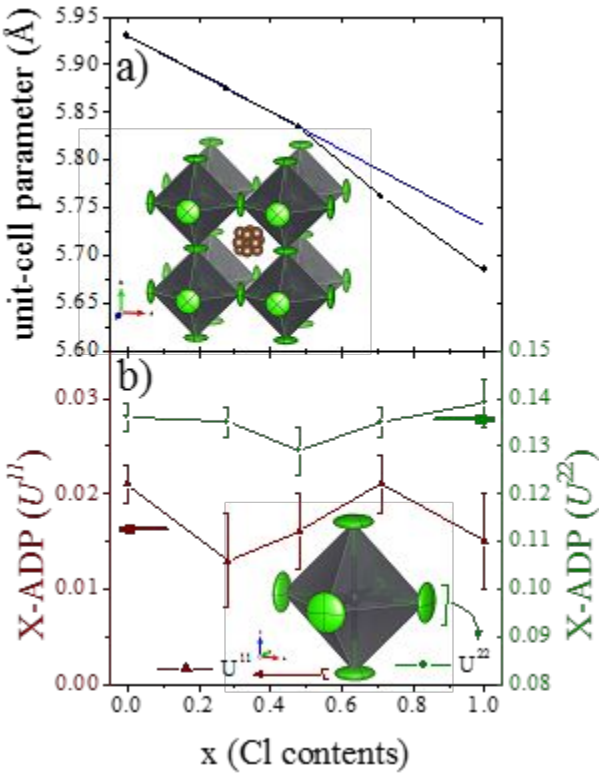

Fig. 5. Unit-cell parameters and anisotropic atomic displacement parameters (ADP) of X site.

Anyhow, these anomalies may be due to the structural disorder introduced by the mixture of halides, for x = 0.33, 0.5 and 0.67. This disorder may affect the ADPs and generates a distribution of interactions between the inorganic PbX_6 skeleton and the methyl-ammonium units, which are not present in $MAPbBr_3$ and $MAPbCl_3$, containing single halide ions. This can be visualized from a statistical distribution of the halide environment of MA groups as shown in Fig. 6. This figure plots the probability (y-axis) for a particular halide distribution around MA units (x-axis) in the different samples. For the end members this probability is 100%, since all MA units are coordinated to 12 Br or Cl atoms. The insert includes illustrative schemes of the extreme situations in comparison with an intermediate case where the MA is coordinated to eight chlorides and four bromides, y =

8. These distributions reveal the high structural disorder given in mixed situations, in contrast to both end members. These probably induce tensions in the lattice preventing a linear behaviour between the pure bromine and chlorine compounds.

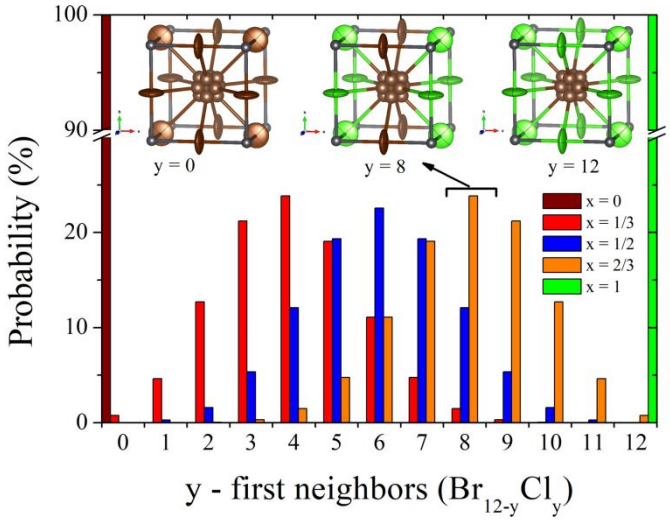

Fig. 6. Statistical probability distribution of the halide environment in $CH_3NH_3Pb(Cl_{1-x}Br_x)_3$ (x = 0, 0.33, 0.5, 0.67 and 1).

3.3. *Low-temperature transitions*

The low-temperature crystal structures of some members of the series (x= 0, 0.5, 0.66, 1) were also investigated from SXRD data, in the 120-300 K temperature range. For both end members, $MAPbBr_3$ and $MaPbCl_3$, phase transitions lowering the symmetry from cubic to tetragonal (X= Br only) and then to orthorhombic (X= Br and Cl) have been observed, with a concomitant decrease of the delocalization of the methyl-ammonium group as symmetry decreases[11, 20-23]. In contrast, for the mixed halide compositions no phase transitions have been detected, obtaining cubic structures ($Pm\bar{3}m$) for the specimens cooled down to 120 K, as illustrated in Figure 7, where the thermal variation of the unit-cell parameters are represented. For x= 0.5 and 0.67 the SXRD patterns corresponding to the cubic structures are collected at T= 120 K, only affected by the expected thermal

contraction. The crystallographic data and Rietveld plots at low temperatures are included in Tables S1-S2 and Figures S1-S6, respectively (Supporting Information).

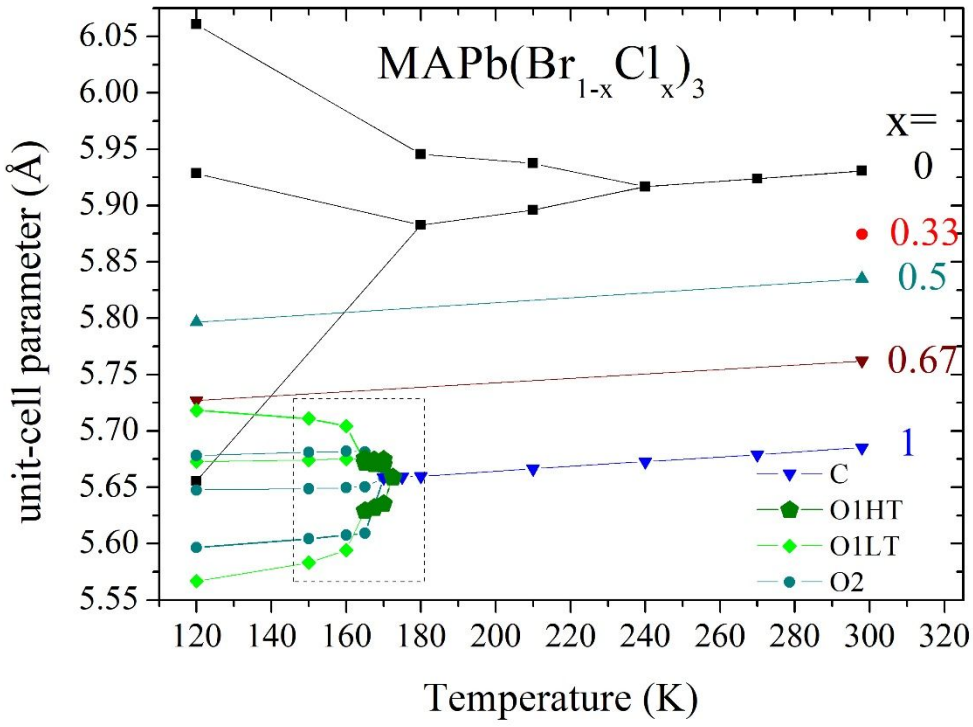

Fig. 7. Thermal evolution of the unit-cell parameters of the $MAPb(Br_{1-x}Cl_x)_3$ perovskites in the 120-300 K temperature region. Only the end members experience phase transitions with symmetry lowering. The $MAPbBr_3$ data taken from Ref [11]

$MAPbBr_3$ presents three polymorphs between 298 to 120 K: cubic ($Pm\bar{3}m$) (298, 270 and 240 K), tetragonal ($I4/mcm$) (210 and 180 K) and orthorhombic ($Pnma$) (120 K).[11] These phases were also reported by other authors from single crystal data.[24-25] In $MAPbCl_3$, the cubic symmetry remains stable down to 180 K. However, the SXRD patterns at 120 and 150 K, exhibit conspicuous reflection splittings as illustrated in Fig. 8. Poglitsch *et al.* reports that this compound presents two phase transitions: $P222_1$ ←(173 K)→ $P4/mmm$ ←(179 K)→ $Pm\bar{3}m$.[21] Later, Chi *et al.* found that the orthorhombic polymorph presents a *Pnma* space group, but with a doubled unit-cell with respect to the cubic aristotype ($a \approx b \approx c \approx 2a_p$).[23] Our patterns (see Fig 8) at 120 and 150 K present diffraction lines compatible with the model reported by Chi *et al.*; however, the preliminary refinements were not

satisfactory, since they showed additional lines that match with a second orthorhombic (*Pnma*) phase similar to that observed in $MAPbBr_3$ ($a \approx \sqrt{2}a_p$; $b \approx 2a_p$; $c \approx \sqrt{2}a_p$). The coexistence of both orthorhombic phases allows an acceptable refinement in the patterns collected at 150 and 120 K. The differences observed in both orthorhombic models reside in the peak width; the conventional *Pnma* phase presents a greater broadening than the doubled *Pnma* structure. This may suggest that the phase mixture is induced by microstructural features.

Due to the observed phase mixtures at low temperature, the mechanism or transient state from cubic to orthorhombic symmetry has been partially known until now. As mentioned above, a transient tetragonal phase (*P*4/*mmm*) was described in a very narrow range of temperature, 172.9-178.8 K.[21] In the search for this intermediate phase, several patterns were collected sequentially close to this temperature range in intervals of 2.5 K, as illustrated in Figure 8, and indeed a transitory phase was identified at 167.5 K. This pattern was initially fitted to a tetragonal model, however, additional diffraction lines were observed, evidencing a true orthorhombic symmetry. A good fit was achieved with the *Pnma* model ($a \approx \sqrt{2}a_p$; $b \approx 2a_p$; $c \approx \sqrt{2}a_p$) similar to that observed at 120, 150 and 160 K, but the unit-cell parameters are substantially less split than those found at lower temperatures. The temperature evolution of the unit-cell parameters is illustrated in Figure 9.

From these facts, is possible to deduce that our chlorine phase presents a more complex transition than that reported previously. In summary, we observe three phases: cubic, orthorhombic ($a \approx \sqrt{2}a_p$; $b \approx 2a_p$; $c \approx \sqrt{2}a_p$) and a second orthorhombic ($a \approx 2a_p$; $b \approx 2a_p$; $c \approx 2a_p$), labelled in Figure 9 as C, O1 and O2, respectively. Additionally, the O1 phase splits in two states with different distortion degree, $O1^{HT}$ and $O1^{LT}$. In the first case, the unit-cell parameters splitting with respect to the cubic a_p is substantially lower than the second case. $O1^{LT}$ is the main phase observed at 167.5 K. In this transient phase, $c/\sqrt{2}$ and $b/2$ are very similar (Fig. 9), which explains the confusion with a tetragonal lattice in the early literature. This is, indeed, a pseudo-tetragonal phase. This complex behaviour also involves an inversion between $b/2$ and $c/\sqrt{2}$ parameters upon cooling, as displayed in Figure 9. The bottom panel of Figure 9 shows the percentage of each phase in this narrow

temperature range. The goodness of the final refinement is included in the SI for all the temperatures (Table S2; Figures S7-S14).

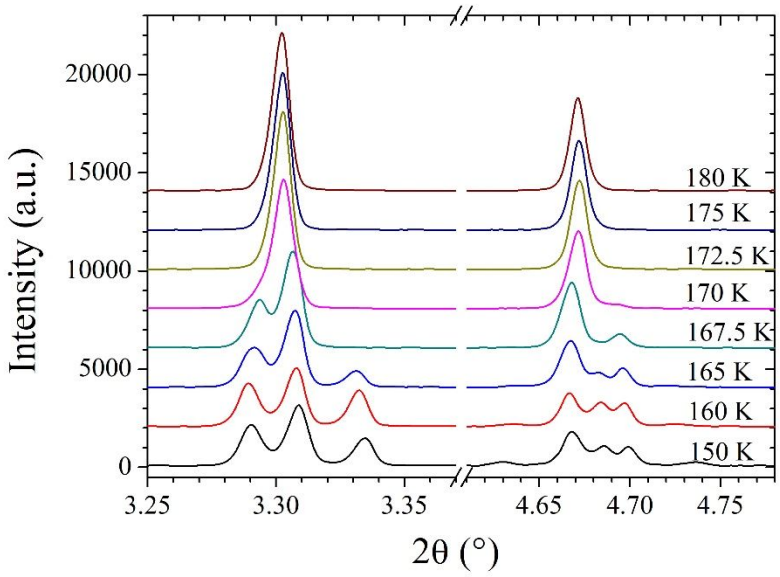

Fig. 8. Selected angular region of the SXRD (λ= 0.3252 Å) spectra of $MAPbCl_3$ at increasing temperatures, illustrating the evolution and splitting of some characteristic reflections.

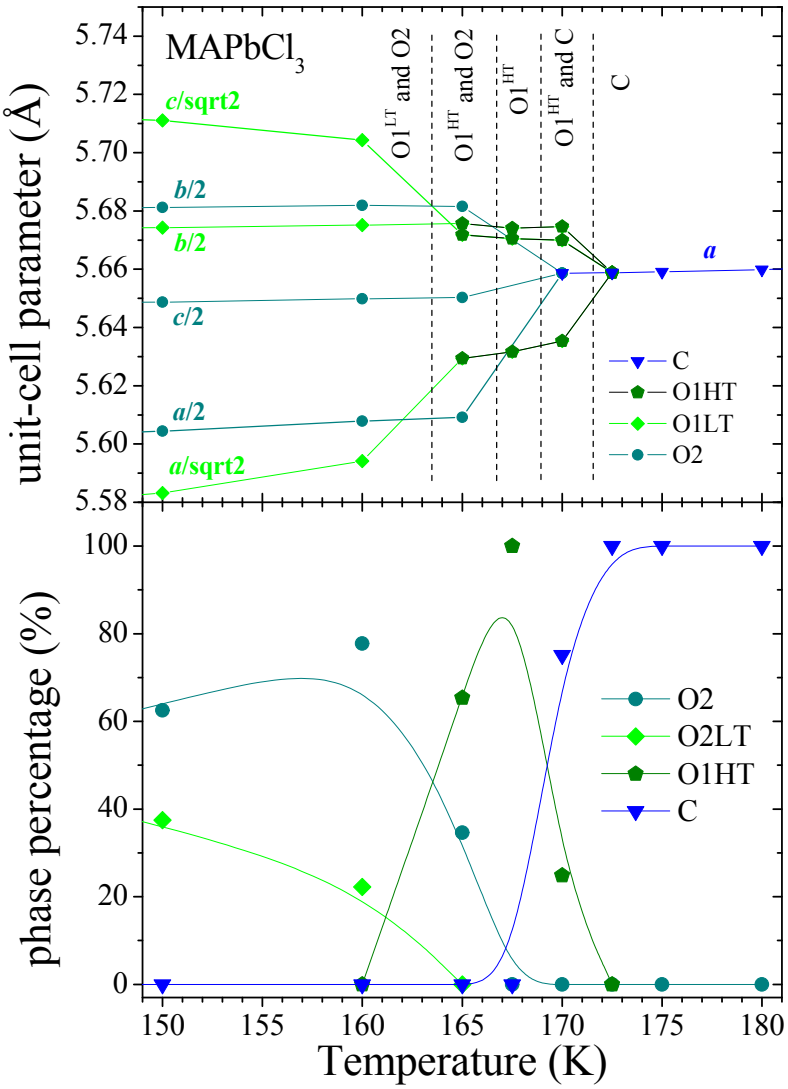

Fig. 9. Thermal evolution of the unit-cell parameters of the $MAPbCl_3$ perovskite in the 150-180 K temperature region. The cubic and the two orthorhombic phases, are labelled C, O1 and O2, respectively. O1 is split in $O1^{HT}$ and $O1^{LT}$ phases. O1HT is strongly pseudo-tetragonal. The lower panel shows the relative abundance of these phases.

On the other hand, an important observation is the absence of phase transitions in the mixed halides down to 120 K. This is not expected considering that the cubic polymorphs are only stable above 179 and 237 K for $MAPbCl_3$ and $MAPbBr_3$, respectively.[21] This unexpected behaviour can be related to the anion disorder introduced in mixed halide

phases. As previously discussed, the organic-inorganic interactions are dramatically different between the intermediate and the end members of the present series, as suggested in Fig 6. Furthermore, the halide disorder may also prevent the cooperative rearrangements needed to drive the octahedral tilt that finally leads to a phase transition.

3.3. *Optical gap by UV-Vis spectra*

Diffuse reflectance UV-Vis spectra, represented in the Fig. 10, were used to calculate the optical absorption coefficient (α) according to the Kubelka–Munk equation:

$$F(R) = \alpha = (1 - R)^2/(2R) \qquad (1)$$ where R is the reflectance (%).

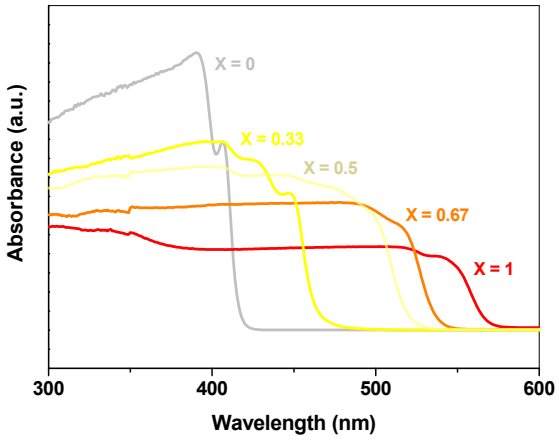

Fig. 10. Absorbance *vs* wavelength of the incident radiation for $MAPb(Br_{1-x}Cl_x)_3$. The gradual evolution in the absorption edge is consistent with the continuous structural change observed by SXRD.

For instance, for $CH_3NH_3PbBr_3$ powder the optical gap is determined to be 2.20 eV from the extrapolation of the linear part of the transformed Kubelka–Munk spectrum with the hν axis. This value increases with the incorporation of chloride ions into the structure (Table 2). The increase in the band gap as Br is replaced by Cl, is generally expected due to the reduced covalency of the lead-halide bonds within the network of $Pb–X_6$ (X = Cl, Br) corner-sharing octahedra.[14]

It is noteworthy that the evolution of the band gap energy (E_g) with the composition is not linear, and the deviation from linearity recalls that observed in the unit-cell parameters evolution at RT, see Figure 11. An additional comparison of E_g with the Pb-X distances also exhibits a non-linear behavior (inset of Figure 11), unveiling that the evolution of E_g is not very much related to the features of the inorganic framework. This observation seems to confirm that the increase in the E_g with the amount of Cl^- derives from the effect on the MA units of the shrinking of the lattice upon the incorporation of smaller Cl^- anions.

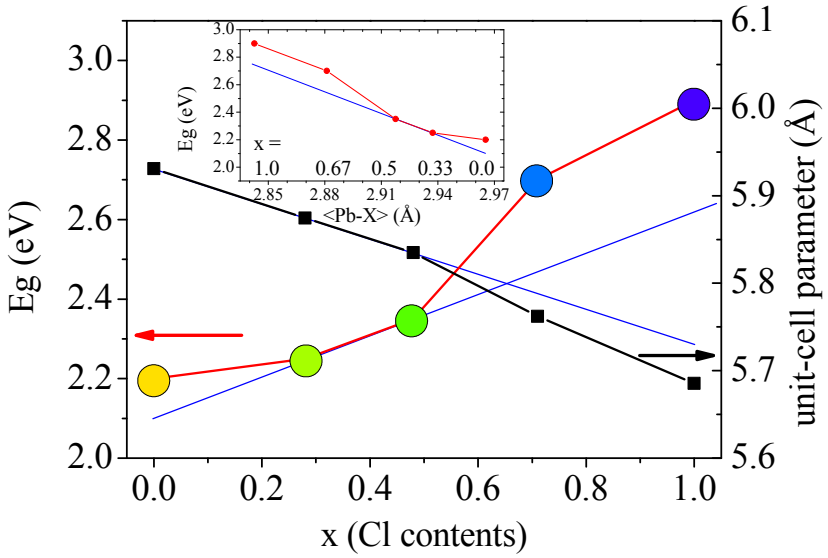

Fig. 11: Comparison between the band gap energy and unit-cell parameter in $MAPb(Br_{1-x}Cl_x)_3$, as a function of the Cl content, x. The colour in the circles corresponds to the band gap energy.

Conclusions

We have synthesized mixed inorganic-organic hybrid halide perovskites based on chlorine and bromine halide anions $CH_3NH_3Pb(Br_{1-x}Cl_x)_3$ (x = 0, 0.33, 0.5, 0.67 and 1). The crystal structures were reported at room temperature as cubic in the space group $Pm\bar{3}m$, and the band gap of these perovskites can be controllably tuned. Whereas both end-members exhibit conspicuous phase transitions, lowering the symmetry from cubic (RT) to tetragonal and orthorhombic, down to 120 K, the mixed-halide phases remain cubic down to this

temperature. This suggests that the halide disorder prevents the cooperative rearrangements needed to drive the octahedral PbX_6 tiltings, which finally lead to phase transitions with a progressive localization of the organic CH_3-NH_3^+ cation.

Supporting Information. Tables with the crystallographic parameters and Rietveld plots from SXRD data for the different compositions at different temperatures.

Acknowledgments

Authors acknowledge financial support given by KIC RAW MATERIALS from European Union (OPTNEWOPT project) and the Spanish Ministry of Economy and Competitiveness (ENE2014-52158-C2-1-R project and MAT2017-84496-R) co-founded by FEDER. C.A.L. acknowledges ANPCyT and UNSL for financial support (projects PICT2014-3576 and PROICO 2-2016), Argentine. C.A.L. is a member of CONICET.

References

1. Dubey, A.; Adhikari, N.; Mabrouk, S.; Wu, F.; Chen, K.; Yang, S.; Qiao, Q., A strategic review on processing routes towards highly efficient perovskite solar cells. *Journal of Materials Chemistry A* **2018,** *6*, 2406-2431.
2. Yang, W. S.; Park, B.-W.; Jung, E. H.; Jeon, N. J.; Kim, Y. C.; Lee, D. U.; Shin, S. S.; Seo, J.; Kim, E. K.; Noh, J. H.; Seok, S. I., Iodide management in formamidinium-lead-halide–based perovskite layers for efficient solar cells. *Science* **2017,** *356*, 1376-1379.
3. Yen, H.-J.; Liang, P.-W.; Chueh, C.-C.; Yang, Z.; Jen, A. K. Y.; Wang, H.-L., Large Grained Perovskite Solar Cells Derived from Single-Crystal Perovskite Powders with Enhanced Ambient Stability. *ACS Applied Materials & Interfaces* **2016,** *8*, 14513-14520.
4. Sadhukhan, P.; Kundu, S.; Roy, A.; Ray, A.; Maji, P.; Dutta, H.; Pradhan, S. K.; Das, S., Solvent-Free Solid-State Synthesis of High Yield Mixed Halide Perovskites for Easily Tunable Composition and Band Gap. *Crystal Growth & Design* **2018,** *18*, 3428-3432.
5. Xing, G.; Mathews, N.; Lim, S. S.; Yantara, N.; Liu, X.; Sabba, D.; Grätzel, M.; Mhaisalkar, S.; Sum, T. C., Low-temperature solution-processed wavelength-tunable perovskites for lasing. *Nature Materials* **2014,** *13*, 476.
6. Tan, Z.-K.; Moghaddam, R. S.; Lai, M. L.; Docampo, P.; Higler, R.; Deschler, F.; Price, M.; Sadhanala, A.; Pazos, L. M.; Credgington, D.; Hanusch, F.; Bein, T.; Snaith, H. J.; Friend, R. H., Bright light-emitting diodes based on organometal halide perovskite. *Nature Nanotechnology* **2014,** *9*, 687.

7. Dou, L.; Yang, Y.; You, J.; Hong, Z.; Chang, W.-H.; Li, G.; Yang, Y., Solution-processed hybrid perovskite photodetectors with high detectivity. *Nature Communications* **2014,** *5*, 5404.
8. Maculan, G.; Sheikh, A. D.; Abdelhady, A. L.; Saidaminov, M. I.; Haque, M. A.; Murali, B.; Alarousu, E.; Mohammed, O. F.; Wu, T.; Bakr, O. M., CH3NH3PbCl3 Single Crystals: Inverse Temperature Crystallization and Visible-Blind UV-Photodetector. *The Journal of Physical Chemistry Letters* **2015,** *6*, 3781-3786.
9. Luo, J.; Im, J.-H.; Mayer, M. T.; Schreier, M.; Nazeeruddin, M. K.; Park, N.-G.; Tilley, S. D.; Fan, H. J.; Grätzel, M., Water photolysis at 12.3% efficiency via perovskite photovoltaics and Earth-abundant catalysts. *Science* **2014,** *345*, 1593-1596.
10. Yang, J.; Siempelkamp, B. D.; Liu, D.; Kelly, T. L., Investigation of CH3NH3PbI3 Degradation Rates and Mechanisms in Controlled Humidity Environments Using in Situ Techniques. *ACS Nano* **2015,** *9*, 1955-1963.
11. López, C. A.; Martínez-Huerta, M. V.; Alvarez-Galván, M. C.; Kayser, P.; Gant, P.; Castellanos-Gomez, A.; Fernández-Díaz, M. T.; Fauth, F.; Alonso, J. A., Elucidating the Methylammonium (MA) Conformation in MAPbBr3 Perovskite with Application in Solar Cells. *Inorganic Chemistry* **2017,** *56*, 14214-14219.
12. Kedem, N.; Brenner, T. M.; Kulbak, M.; Schaefer, N.; Levcenko, S.; Levine, I.; Abou-Ras, D.; Hodes, G.; Cahen, D., Light-Induced Increase of Electron Diffusion Length in a p–n Junction Type CH3NH3PbBr3 Perovskite Solar Cell. *The Journal of Physical Chemistry Letters* **2015,** *6*, 2469-2476.
13. Wang, L.; Wang, K.; Xiao, G.; Zeng, Q.; Zou, B., Pressure-Induced Structural Evolution and Band Gap Shifts of Organometal Halide Perovskite-Based Methylammonium Lead Chloride. *The Journal of Physical Chemistry Letters* **2016,** *7*, 5273-5279.
14. Comin, R.; Walters, G.; Thibau, E. S.; Voznyy, O.; Lu, Z.-H.; Sargent, E. H., Structural, optical, and electronic studies of wide-bandgap lead halide perovskites. *Journal of Materials Chemistry C* **2015,** *3*, 8839-8843.
15. Wang, C.; Tang, Y.; Hu, Y.; Huang, L.; Fu, J.; Jin, J.; Shi, W.; Wang, L.; Yang, W., Graphene/SrTiO3 nanocomposites used as an effective electron-transporting layer for high-performance perovskite solar cells. *RSC Advances* **2015,** *5*, 52041-52047.
16. Wu, Z.; Bai, S.; Xiang, J.; Yuan, Z.; Yang, Y.; Cui, W.; Gao, X.; Liu, Z.; Jin, Y.; Sun, B., Efficient planar heterojunction perovskite solar cells employing graphene oxide as hole conductor. *Nanoscale* **2014,** *6*, 10505-10510.
17. Baikie, T.; Fang, Y.; Kadro, J. M.; Schreyer, M.; Wei, F.; Mhaisalkar, S. G.; Graetzel, M.; White, T. J., Synthesis and crystal chemistry of the hybrid perovskite (CH3NH3)PbI3 for solid-state sensitised solar cell applications. *Journal of Materials Chemistry A* **2013,** *1*, 5628-5641.
18. Fauth, F.; Boer, R.; Gil-Ortiz, F.; Popescu, C.; Vallcorba, O.; Peral, I.; Fullà, D.; Benach, J.; Juanhuix, J., The crystallography stations at the Alba synchrotron. *The European Physical Journal Plus* **2015,** *130*, 160.
19. Rodriguez-Carvajal, J.; Roisnel, T., Recent advances in magnetic structure determination by neutron powder diffraction. *Physica B* **1993,** *192*, 55-69.
20. Onoda-Yamamuro, N.; Matsuo, T.; Suga, H., Dielectric study of CH3NH3PbX3 (X = Cl, Br, I). *Journal of Physics and Chemistry of Solids* **1992,** *53*, 935-939.

21. Poglitsch, A.; Weber, D., Dynamic disorder in methylammoniumtrihalogenoplumbates (II) observed by millimeter-wave spectroscopy. *The Journal of Chemical Physics* **1987,** *87*, 6373-6378.
22. Maaej, A.; Bahri, M.; Abid, Y.; Jaidane, N.; Lakhdar, Z. B.; Lautié, A., Raman study of low temperature phase transitions in the cubic perovskite CH3NH3PbCI3. *Phase Transitions* **1998,** *64*, 179-190.
23. Chi, L.; Swainson, I.; Cranswick, L.; Her, J.-H.; Stephens, P.; Knop, O., The ordered phase of methylammonium lead chloride CH3ND3PbCl3. *Journal of Solid State Chemistry* **2005,** *178*, 1376-1385.
24. Baikie, T.; Barrow, N. S.; Fang, Y.; Keenan, P. J.; Slater, P. R.; Piltz, R. O.; Gutmann, M.; Mhaisalkar, S. G.; White, T. J., A combined single crystal neutron/X-ray diffraction and solid-state nuclear magnetic resonance study of the hybrid perovskites CH3NH3PbX3 (X = I, Br and Cl). *Journal of Materials Chemistry A* **2015,** *3*, 9298-9307.
25. Mashiyama, H.; Kawamura, Y.; Kasano, H.; Asahi, T.; Noda, Y.; Kimura, H., Disordered Configuration of Methylammonium of CH3NH3PbBr3 Determined by Single Crystal Neutron Diffractometry. *Ferroelectrics* **2007,** *348*, 182-186.

Tables

Table 1: Crystallographic data for $MAPb(Br_{1-x}Cl_x)_3$ with x = 0, 1/3, 1/2, 2/3 and 1 at room temperature from synchrotron XRPD.

$MAPb(Br_{1-x}Cl_x)_3$	x = 0 [Ref. 11]	x = 1/3	x = 1/2	x = 2/3	x = 1
a (Å)	5.93076(2)	5.8745(1)	5.83502(7)	5.76205(7)	5.68532(4)
Pb (1*a*) (0,0,0)					
$U^{11}=U^{22}=U^{33}$	0.0236(5)	0.027(1)	0.0336(7)	0.0265(4)	0.0236(4)
$Br_{1-x}Cl_x$ (3*d*) (0.5,0,0)					
x	0	0.28(3)	0.48(2)	0.71(1)	1
U^{11}	0.021(2)	0.013(5)	0.016(4)	0.021(3)	0.015(5)
$U^{22}=U^{33}$	0.136(3)	0.135(7)	0.129(5)	0.135(3)	0.139(5)
C/N (6*f*) (0.5,*y*,*y*)					
y	0.42(1)	0.597(6)	0.597(4)	0.597(2)	0.592(4)
U_{iso}*/U_{eq}	0.03(5)	0.01(4)*	0.02(3)*	0.02(1)*	0.04(2)*

Rp(%)	12.3	15.9	13.9	11.6	13.0
Rwp(%)	16.2	20.3	17.8	14.4	16.9
χ^2	2.1	1.1	1.4	1.8	1.3
R_{Bragg}(%)	7.7	15.2	8.3	5.4	7.6

Impurities :
$MAPbCl_3$: 12.2(4)% $PbCl_2$ y 9(1)% MACl
$MAPbBrCl_2$: 0%
$MAPbBr_{1.5}Cl_{1.5}$: 20.4(4)% $PbCl_2$
$MAPbBr_2Cl$: 13.4(4)% $PbCl_2$

Table 2: Band gap (E_g) of the perovskites

Perovskite	E_g (eV)
$CH_3NH_3PbBr_3$	2.20
$CH_3NH_3PbBr_2Cl$	2.25
$CH_3NH_3PbBr_{1.5}Cl_{1.5}$	2.35
$CH_3NH_3PbBrCl_2$	2.70
$CH_3NH_3PbCl_3$	2.90

For Table of Contents Use Only

Crystal growth, structural phase transitions and optical gap evolution of $CH_3NH_3Pb(Br_{1-x}Cl_x)_3$ powders

M. C. Alvarez-Galván, J. A. Alonso, C.A. López, E. López-Linares, C. Contreras, M.J. Lázaro, F. Fauth and M.V. Martínez-Huerta

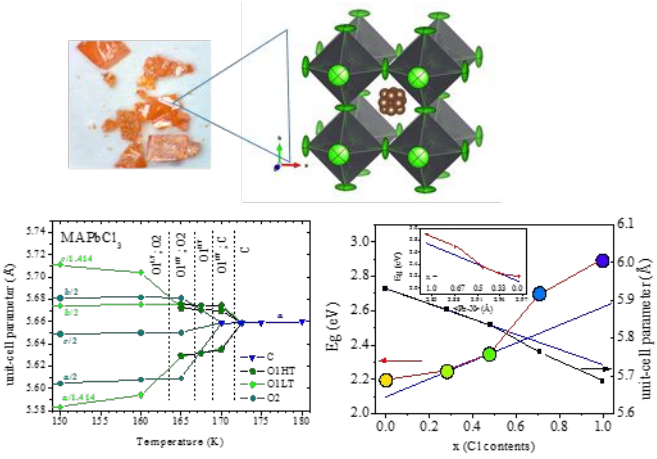

Both end-members exhibit conspicuous phase transitions, from cubic (RT) to tetragonal and orthorhombic, down to 120 K, whereas the mixed-halide phases remain cubic: the halide disorder prevents the cooperative rearrangements needed to drive the octahedral PbX_6 tiltings. The band gap can be controllably tuned; the deviation from linearity follows the unit-cell parameters evolution: the increase in the E_g is closely correlated to the collapse of the lattice upon the incorporation of smaller Cl^- anions.